

Characterization of sinter flue dust to enhance alternative recycling and environmental impact at disposal

*Victoria Masaguer^a, Paula Oulego^b, Sergio Collado^b, María A. Villa-García^c, and
Mario Díaz^{b,*}*

^aGlobal R&D Asturias Centre “GRID”, Apartado 90, 33400 Aviles, Spain

^bDepartment of Chemical and Environmental Engineering, University of Oviedo,

c/Julián Clavería s/n, E-33071, Oviedo, Spain

^cDepartment of Organic and Inorganic Chemistry, University of Oviedo

c/Julián Clavería s/n, E-33071, Oviedo, Spain

*Corresponding author's e-mail: mariodiaz@uniovi.es

*Phone: +34 985 10 34 39; Fax: +34 985 10 34 34

ABSTRACT

Dust emission is one of the main environmental pollution impacts associated with steelmaking. In this sense, electrostatic precipitators (ESP) are regarded as the best available technique for treating this type of emission, thus generating two differentiated fractions: coarse and fine. Thorough chemical and structural characterization of both materials was carried out to recycle these byproducts in either the sintering process or other steps of pig iron production. Both types of dusts are crystalline heterogeneous materials mainly composed of sepiolite ($\text{Mg}_8\text{Si}_{12}(\text{OH})_2 \cdot 12\text{H}_2\text{O}$), hematite (Fe_2O_3) and calcite (CaCO_3), the coarse fraction containing low amounts of Na ($0.38 \pm 0.04\%$) and K ($0.17 \pm 0.02\%$), which adversely affect blast furnace operation. Hence, the coarse fraction is suitable for recycling, whereas the fine one presents higher concentrations of these alkali elements. Besides, textural characterization revealed that dust particulates are essentially macroporous materials, with specific surface area values of $21.6 \text{ m}^2/\text{g}$ for the coarse fraction and $33.7 \text{ m}^2/\text{g}$ for dust fines. In order to ensure inoffensive dumpsites, the environmental behavior associated with dust particles accumulated in disposal areas was also evaluated by performing leaching studies simulating different rainfall scenarios. It was found that the specific leaching rates of Ca, Mg, K and S varied between 0.072 ± 0.001 and $0.75 \pm 0.01 \mu\text{g}_{\text{element}}/(\text{g}_{\text{dust}} \cdot \text{d})$, whereas slower leaching rates were obtained for heavy metals (Fe, Mn and Cu), the values ranging from $(1.20 \pm 0.1) \times 10^{-4}$ to $(1.8 \pm 0.1) \times 10^{-3} \mu\text{g}_{\text{element}}/(\text{g}_{\text{dust}} \cdot \text{d})$. These low rates indicate that the leaching of sinter dusts compounds has minimal environmental impact.

Keywords: characterization, dust abatement, environmental impact, heavy metals, leaching, sinter dusts.

1. INTRODUCTION

In the steel making industry, all the processing steps which involve handling, crushing, charging, screening or transporting the raw materials cause continuous dust emissions. Dust is thereby one of the main environmental impacts of steelmaking and creates pollution both inside and outside the plant (Pelino et al., 2012). This source of pollution includes sinter emissions, such as sinter dust with particulate matter and various gases: CO, CO₂, SO_x and NO. The outcome is a potential increase in the concentration of suspended particles in the air, mainly inside the factory, if these emissions are not treated efficiently. Over the last decades, the use of new technology has significantly reduced the amount of dust generated by a typical steel plant (Rabah, 1999). The emissions are usually collected and encapsulated in housing with suction hoods that are directly connected to cleaning devices. Cleaning of sinter off-gases is mainly achieved by dust abatement (BREF, 2012). Electrostatic precipitators (ESPs) are the most widely used abatement systems for dust emissions. Other alternatives rely on the use of cyclones, web scrubbers or fabric/baghouses filters. Nevertheless, ESPs are often preferred due to their simple design, low operating costs, high collection efficiency and low pressure drop (Vehlow, 2015; Bohidar et al., 2015). Usually, they consist of dry devices with three or four fields installed in sinter plants located within the European Union (Remus et al., 2013), and can reduce dust emissions with efficiencies above 95% and, in some cases, can yield final dust concentrations in the range of 20 to 50 mg/Nm³ during normal operation periods, excluding start-ups and shutdowns (Reyes and Elholm, 2011). Therefore, adequate design and sound guidelines for the correct maintenance of advanced ESPs are necessary to ensure good performance, since this technique is considered the best available one (BAT) to reduce daily dust particulates emission.

Electrostatic precipitators are originally designed for sinter plants basing on both the gas and dust properties, making it necessary to conduct an in-depth study on dust characteristics, such as mineral composition and chemical behavior. The coarse fraction of the dust, which is prone to efficient separation by ESPs, results from the first part of the strand, and originates from the sinter feed and the lower layer. Dust fines are formed in the sintering zone, after the evaporation of water from the mixture is accomplished.

Since the physicochemical properties of the dust particles formed in the sinter plant are key parameters for suitable performance and efficiency of the electrostatic precipitators, their design requires a detailed study of the dust particulates characteristics. This study is part of a project led by ArcelorMittal, whose aim is to gain in-depth knowledge of the physicochemical properties of sinter dusts in order to find alternative uses to recycle them and develop highly efficient ESPs. Due to the new legislation and its impact on the waste management policies in Europe, efforts are driven to reduce the environmental and health impacts of waste and disposal activities and are also focused on improving Europe's efficiency in terms of resource utilization. To achieve these goals, it is required much higher levels of recycling and minimization of the consumption of natural resources according to 7th Environment Action Program of European Commission.

In this work, the study of the chemical and mineralogical composition and evaluation of the textural and morphological properties of such byproducts were carried out using a variety of techniques: XRF, XRD, elemental analysis, FTIR spectroscopy, TGA-DTG analysis, N₂ adsorption-desorption, Hg intrusion porosimetry, SEM and TEM. To the best of our knowledge, sinter dusts were previously characterized in just a few works (Chang et al., 2015; Lanzerstorfer and Steiner, 2016; Sinha et al., 2010) but such characterization

was cursory in comparison with the one here presented, in which a great number of techniques were employed. Besides, this work addressed, for the first time ever, the study of the environmental behavior of dust particles accumulated in disposal sites for ensuring environmentally-friendly sinter dust dumpsites. Thus, the changes in the chemical composition of dust particulates, which were previously treated under simulated environmental conditions, were thoroughly analyzed.

2. MATERIALS AND METHODS

2.1. Experimental Section

The samples of sinter dusts employed in this work were provided by an ArcelorMittal sinter plant located in Asturias (north of Spain), namely ArcelorMittal Veriña, and consisted of two fractions collected from different fields of the ESPs module corresponding to the sinter dust fine fraction (sample FF) and the sinter dust coarse fraction (sample CF). The samples were collected by qualified plant personnel for several weeks of dust production in order for it to be representative. Prior to the characterization, it was necessary to mill and sieve the sample CF and sieve the FF one, except in the case of N₂ adsorption-desorption analysis, in which the samples were used without modification. In both cases, the fraction with sizes below 75 microns was used. In the environmental tests, the samples FF and CF were also employed without modification.

2.2. Characterization Methods

Shimadzu EDX-720 energy dispersive X-Ray fluorescence (XRF) spectrometer was used to determine the chemical composition of sinter dusts. The content of C, H, N and S was measured by elemental analysis employing an Elementar Vario EL analyzer. Powder X-ray diffraction (XRD) patterns were obtained at room temperature in order to determine the mineralogical composition of the samples. PANalyticalX'Pert Pro powder

diffractometer using Cu K α radiation ($\lambda_{K\alpha} = 1.5406 \text{ \AA}$) and a graphite secondary monochromator was employed. The diffractograms were recorded for 2θ values between 5° and 80° by 0.02° step, with a scan step time of 1 s. Quantitative phase analysis was carried out using the Rietveld refinement method (Taylor, 2001). FTIR spectra of the samples were recorded in the $4000 - 400 \text{ cm}^{-1}$ range, by means of a Perkin-Elmer PARAGON 1000 spectrometer. The resolution employed was 4 cm^{-1} . The samples were pressed into small discs using a spectroscopically pure KBr matrix. Thermal analysis was carried out using a Mettler Toledo TGA/SDTA851e thermogravimetric analyzer. 45 – 47 mg of each of the samples were heated in alumina crucibles under a nitrogen atmosphere at a heating rate of $10^\circ\text{C}/\text{min}$ from 20°C to 1000°C . Textural properties (specific surface area and porous structure) were studied by nitrogen adsorption-desorption at 77 K using a Micromeritics ASAP 2020 instrument. Prior to the analysis, it was necessary to degas the dusts (400-450 mg) at 120°C for 10 h. The presence of macroporosity was determined through Hg intrusion porosimetry using a Micromeritics Autopore IV instrument. The analysis was carried out with a sample mass of 950 mg at low and high pressure (0.1-60000 psi) employing a penetrometer bulb for powdered materials. The morphological characterization of the sinter dusts and energy dispersive X-ray analyses (EDX) was performed using a JEOL JMS-6610LV scanning electron microscope (SEM) operating at 0.3–30 kV. Previously to the SEM characterization and EDX analysis, the samples were sputtered coated with gold. Transmission electron microscopy (TEM) was performed on a MET JEOL-2000 EX-II microscope operating at 160 kV. Samples were prepared by sonicating the powdered sample in ethanol and then evaporating several drops of suspension on copper grids.

2.3. Environmental behavior

Leaching tests were performed at room temperature (20°C) in a double-neck flat bottom glass flasks of 250 mL. Three different liquid (L) to solid (S) ratios were studied: 10, 2.5 and 1.25 mL/g. Such L/S ratios were selected in order to simulate intense, medium and low rainfall conditions, respectively. In all cases, 150 mL of distilled water (as rainfall water) were added to the proper amount of sinter sample to give the desired L/S ratio. The mixture of water and sinter sample was stirred very slowly (50 rpm) in order to guarantee the homogeneity of the suspension. The mixture was kept under constant stirring and samples were taken at 4 different times in order to simulate various storage times: i) 1 week, ii) 1 month, iii) 3 months and iv) 6 months. After such periods, the mixture was centrifuged at 10000 g for 10 min in order to separate the polluted water from the solid. The polluted water was filtered through a PVDF membrane (pore size of 0.45 µm) to remove any remaining solids before the analysis of the leached elements. The analysed elements were alkali metals (K), alkaline earth metals (Ca, Mg), heavy metals (Cu, Fe and Mn), metals (Al), halogens (Br) and non-metallic elements (S). These elements were determined by ICP mass spectrometry (ICP-MS), using an Agilent 7500ce Spectrometer. Rhodium (^{103}Rh) was used as the internal standard.

3. RESULTS AND DISCUSSION

3.1. Sample Characterization.

3.1.1. Chemical Composition.

Elemental analysis of samples FF and CF (see Table 1) showed that the presence of both nitrogen and sulfur compounds is negligible in both dusts. Carbon content is low in sample CF (3.67% ± 0.03), whereas it is significant in sample FF (11.74% ± 0.02). This can be due to the carbonation of calcium compounds (such as portlandite ($\text{Ca}(\text{OH})_2$) present in the sinter dust during its storage. In this sense, it was reported that under high

relative humidity conditions (from 75% to 90%), carbonation of Ca(OH)_2 is fostered during the storage phase (López-Arce et al., 2011; Navarro et al, 2011), even at low levels of CO_2 and low temperature (10°C). This can be explained considering that a humid atmosphere seems to act upon Ca(OH)_2 in accordance with the following three sequential steps: i) physical adsorption of the water held within the atmospheric humidity at the Ca(OH)_2 grains surface; ii) this water then allows the Ca(OH)_2 to dissolve into Ca^{2+} and OH^- ions. In addition, the dissolution of CO_2 , under these basic pH conditions, yields CO_3^{2-} ions and iii) these two dissolution steps contribute to the precipitation of CaCO_3 (Dheilly et al., 2002).

Carbonation was favored during both the sampling period and the storage phase, as the average relative humidity were 85% and 80%, respectively

TABLE 1

Chemical composition of the sinter dusts was measured by X-ray fluorescence spectroscopy (XRF). The composition of sample FF was: $54.5\% \pm 0.2 \text{ Fe}_2\text{O}_3$; $24.1\% \pm 0.2 \text{ CaO}$; $8.40\% \pm 0.04 \text{ SiO}_2$; $5.07\% \pm 0.03 \text{ SO}_3$; $2.812\% \pm 0.005 \text{ Cl}$; $2.321\% \pm 0.006 \text{ K}_2\text{O}$; $1.008\% \pm 0.008 \text{ Al}_2\text{O}_3$. In the case of the CF sample, the chemical composition was: $57.6\% \pm 0.4 \text{ Fe}_2\text{O}_3$; $17.8\% \pm 0.2 \text{ CaO}$; $17.5\% \pm 0.2 \text{ SiO}_2$; $2.0\% \pm 0.2 \text{ SO}_3$; $2.30\% \pm 0.05 \text{ MgO}$; $1.52\% \pm 0.05 \text{ Al}_2\text{O}_3$. Hence, iron, calcium and silicon were the main components of sinter dusts. The rest of the constituents were present at low concentration, some of them being traces (see Table 2). It should be noted that the leaching behavior of the components of sinter dusts was studied because of the toxicity inherent to some of them. In this sense, adverse effects have been reported due to exposure to aluminum and manganese (Krewski et al., 2007; Katsnelson et al, 2015; Ljung et al., 2009).

TABLE 2

3.1.2. *Mineralogical Characterization*

Structural characterization of sinter dusts was carried out by means of XRD measurements. The diffraction patterns of the samples CF and FF are depicted in Figure 1. Although quite similar, some differences in the intensity of the diffraction lines of some phases were observed. Such patterns indicated that sinter dusts are highly heterogeneous materials composed of a blend of crystalline phases.

FIGURE 1

Analysis of the different diffraction lines revealed the presence of the following constituents in both samples: hedenbergite ($\text{CaFeSi}_2\text{O}_6$), anhydrite (CaSO_4), sepiolite ($\text{Mg}_8\text{Si}_{12}(\text{OH})_2 \cdot 12\text{H}_2\text{O}$), calcite (CaCO_3), hematite (Fe_2O_3), albite ($\text{NaAlSi}_3\text{O}_8$), quartz (SiO_2), microcline (KAlSi_3O_8), portlandite ($\text{Ca}(\text{OH})_2$) and dolomite ($\text{CaMg}(\text{CO}_3)_2$). Besides, gibbsite ($\text{Al}(\text{OH})_3$) was also identified in sample CF and sylvine (KCl) in sample FF. Phase quantification was performed by applying the Rietveld refinement method to the reflections resulting from the overlapping of different diffraction peaks (Taylor, 2001). The percentage of both major and minor phases present in the samples was calculated, and the obtained values are shown in Table 3. According to these results, the main components of both samples were sepiolite ($26.85 \pm 0.05\%$ for CF and $18.0 \pm 0.2\%$ for FF), hematite ($24.20 \pm 0.03\%$ for CF and $34.9 \pm 0.1\%$ for FF) and calcite ($17.9 \pm 0.1\%$ for CF and $10.48 \pm 0.02\%$ for FF). In sample FF, portlandite was also identified as a major phase ($10.37 \pm 0.03\%$). These results are in agreement with those obtained by XRF, which

showed that iron, calcium and silicon were the major elements found in the sinter particles.

TABLE 3

The most commonly employed method for recycling sinter dust consists of returning it directly to the sintering furnace to benefit from its Fe and C content (Tang et al., 2013). Nevertheless, it should be noted that alkali metals (Na and K) are also reused in the recycling process and these elements have a negative impact on normal blast furnace operations (Peng et al., 2011, 2008; Tang et al., 2015). With the aim of mitigating these harmful effects, some metallurgical plants have introduced limitations on the amount of alkalis allowed in the input materials. The limiting alkali content depends on the steel producer, the upper value varying between 2.5 and 7.5 kg per ton of pig iron (Gridasov et al., 2016). However, in our particular case, the upper experimental limit established by ArcelorMittal is 2.0 kg per ton of pig iron. Besides, Na and K form layers of insulating deposits over the electrodes of ESP units, thus diminishing their removal efficiency. Hence, another dedusting technology could be evaluated. In this sense, fabric filters are a suitable alternative since higher removal efficiencies than those obtained with ESPs can be reached, in particular for the fine fraction of sinter dust. However, it should be noted that the flue gas temperature conditions their feasibility, as fabric filters (mainly made of polymeric materials) withstand temperatures up to 260°C (Vehlow, 2015). In this case, based on experimental data provided by ArcelorMittal, the gas temperatures in both primary (100-150°C) and secondary (70-100°C) sinters are below 260°C, thereby making it possible to employ them. Nevertheless, the disadvantage of fabric filters compared to ESPs lies in their much higher pressure drop (Vehlow, 2015). Furthermore, the use of

fabric filters requires a completely new installation downstream of the ESP unit and the main process fan, and, consequently, higher investment. Considering that the volume of gases in typical sinter plants range from 333,000 Nm³/h to 1,600,000 Nm³/h (Remus et al., 2013), their installation can have a negative impact on both the economy and productivity of the sinter process. Therefore, an economic evaluation is needed before their implementation.

The percentage of Na and K in sample CF was $0.38 \pm 0.04\%$ and $0.17 \pm 0.02\%$, respectively, while in sample FF, the values were $0.51 \pm 0.03\%$ and $1.8 \pm 0.1\%$, respectively. On viewing these data, it would be recommended to recycle the coarse fraction due to its lower content of alkali metals. For this reason, the coarse fraction is currently being reused almost completely. From the total amount of sinter dusts, which are normally generated at a rate of 4 kg/t of steel produced, around 70% is recycled directly in the sintering process, thanks to the suitability of the coarse fraction for such purpose. As previously commented, the remainder (fine fraction), presents a higher alkali content, which can diminish the removal efficiency of ESP units, thus limiting its recyclability without pretreatment. Such pretreatments can be chemical (dissolution) or mechanical (agglomeration), or a combination of the foregoing. In this sense, chemical pretreatment, using brine as solvent, is carried out no more than occasionally due to its high cost. This is the reason why the fine fraction is being disposed of by landfilling. A potential alternative to handle this fraction could consist of wetting grinding combined with sulfidization flotation. This process allows for the recovery of KCl liquor and obtaining raw materials for the metallurgy of Fe, Ag and Pb (Tang et al., 2015). It should be pointed out that its implementation would require a full cost evaluation.

3.1.3. *FTIR Spectroscopy*

This reliable technique provides valuable structural information, and supplies conclusive evidence of the functional groups of the different phases found in the sinter dust. Figure 2 depicts the FTIR spectrum of sample CF, this being practically equal to the spectrum of sample FF (Figure S1 of the supplementary material).

FIGURE 2

The bands found in the region between 3688 and 3550 cm^{-1} corresponds to hydroxyl stretching modes and the band at 980 cm^{-1} was due to hydroxyl deformation modes, which indicates the presence of hydroxides in the dust samples. It should be noted that the heterogeneity of dust samples causes the overlapping of hydroxyl stretching bands, thus hindering the assignment of the hydroxyl vibration modes to different crystalline phases. The absorptions at 3622 cm^{-1} and at 3688 cm^{-1} can be assigned to hydroxyl stretching vibrations of silicates, which present OH groups in their structure (Frost et al., 2004, 1998). The band observed at 3644 cm^{-1} is due to stretching vibrations of hydroxyl group of portlandite. Besides, the absorption bands in the hydroxyl stretching zone at 3622 cm^{-1} and 3550 cm^{-1} is also characteristic of the alumina-water system (Frost et al., 1999). The broad band centered at 3430 cm^{-1} and the peak at 3622 cm^{-1} can be due to: i) hydroxyl stretching modes of hydrated carbonates (Queralt et al., 1997), and ii) water molecules either coordinated or adsorbed. The band at 1654 cm^{-1} is assigned to bending modes of hydroxyl group of the hydrated compounds and hydroxides identified in the dust samples. The presence of carbonates is confirmed by the strong and broad bands observed between 1400 and 1800 cm^{-1} , which are due to C-O stretching modes, and the bands at 874 and 745 cm^{-1} assigned to C-O deformation modes (Mayo et al, 2004). The bands from 1135 cm^{-1} to 980 cm^{-1} are characteristics of the stretching mode of Si-O present in silicates and

SiO₂. Besides, absorption bands typical of OH group vibrations of aluminium and iron oxyhydroxides (Namduri and Nasrazadini, 2008; Van der Marel and Beutelspacher, 1976) can also be found in this zone. The band at 745 cm⁻¹ could be assigned to the stretching vibrations of Al-O (Saniger, 1995), revealing the existence of aluminium compounds, such as gibbsite. FTIR absorptions from 675 to 450 cm⁻¹ are commonly observed in different oxides (Chukanov and Chervonnyi, 2016; Salama et al., 2015; Navarro et al., 2010). Thus, hematite, periclase, ferrites, silicates and most metallic oxides have been identified in this zone. Hematite showed two IR peaks at 476 cm⁻¹ and 540 cm⁻¹, which are due to the stretching vibration of Fe-O (Chukanov and Chervonnyi, 2016; Salama et al., 2015). Peaks at 652 and 668 cm⁻¹ were attributed to various Mg-O-Mg vibration modes of periclase (Isik and Gasanly, 2018). Hedenbergite exhibited a band at 620 cm⁻¹, which can be assigned to bending Si-O-Si vibrations, and a band at 577 cm⁻¹, which probably results from the out-of-plane bending OH vibrations (Jovanovski et al., 2009). The heterogeneous composition of the sinter dust hampers obtaining additional information from this part of the spectrum, due to the overlapping of the characteristic bands of the different components. These components include albite, microcline, gibbsite and sepiolite. In this sense, both albite and microcline exhibited bands at 534 and 648 cm⁻¹ that can be due to the bending vibration of O-Si-O and O-Al-O and the pseudo-lattice or tetrahedral ring vibrations, respectively (Makreski et al., 2009). Gibbsite presents bands in the region from 500 to 650 cm⁻¹, which are characteristic of out-of-plane OH bending vibrations (Schroeder, 2002). Besides, sepiolite shows peaks at 572 and 614 cm⁻¹, which can be attributed to MgO₆ deformation and O-Mg-O bending vibration (McKeown et al., 2002).

This spectroscopic analysis also reveals the presence of the following phases in the dust: iron oxides, calcium and aluminum hydroxide, calcium carbonates and silicates, in agreement with the XRD results.

3.1.4. Textural characterization

Primary dust and sludge generation ratio is known to be in the 0.08-24 kg/t sinter range, the mean value being 0.6 kg/t sinter (World Steel Association, 2010). The sinter plant and blast furnaces are the main recovery routes. Nevertheless, not all the materials are chemically or physically suitable for the internal reuse in the steel making process. Therefore, from an environmental point of view, their potential valorization as low cost adsorbents for wastewater treatment and removal of toxic pollutants should be studied more in-depth in subsequent works. It should be noted that the adsorption behavior is significantly affected by several factors, such as surface area and pore size distribution of the adsorbents, as well as the functional groups present on their surface. Thus, high surface areas are desirable in order to obtain higher uptakes. This is due to the fact that adsorption involves primarily interactions of adsorbate with the atoms of the adsorbent walls (Frost et al., 2006). In addition to this, the pore size distribution of the adsorbent determines the accessibility of the adsorption sites. In this sense, it is clear that the accessibility increases with increasing pore size. However, large pore sizes usually promote leaching, particularly in cases where the interaction adsorbate-adsorbent is weak (Ritter et al., 2010). Consequently, this leads to a compromise between high surface area and suitable pore size distribution.

Regarding the functional groups, the adsorption behavior depends on the type of pollutant. For instance, the presence of oxygen-containing functional groups can increase the adsorption of volatile organic compounds (VOCs) owing to hydrogen bonds and

dipole-dipole interactions between the functional groups and VOCs molecules (Liang et al., 2018). Besides, the operation mode (batch or fixed-bed column) and pH of the effluent must be considered. Therefore, surface area and the kind of porosity should be thoroughly study in order to evaluate the potential uses of sinter dusts as cost-effective adsorbents. Specific surface areas and mesopore size distributions of samples CF and FF are depicted in Figure 3. These values were determined using the nitrogen adsorption-desorption isotherms at 77 K. The isotherms are characteristic of type IV according to the BDDT classification (Brunauer et al., 1940), and exhibit narrow hysteresis loops, which can be classified as type H3. This type of hysteresis loops are characterized by the presence of slit-shaped pores. Both isotherms show a low nitrogen uptake at relative pressures lower than 0.2, which indicated the absence of significant microporosity. Besides, at relative pressures around one, the adsorption limit is not defined clearly, revealing the existence of macroporosity in the solids.

FIGURE 3

The mesopore size distributions were calculated by the method of Barret, Joyner and Halenda (BJH) (Barret et al., 1951). BET specific surface areas (S_{BET}), values of the most frequent pore diameters ($D_{p,max}$) obtained from the pore diameter distribution curves and the cumulative pore volume of each sample (V_p) are depicted in Table 4. Sample FF had higher specific surface area and smaller average mesopore diameters than sample CF, but the cumulative pore volume is higher for sample CF, which can be explained taking into account that wider pores contribute more to volume than to surface.

TABLE 4

Macroporosity of the samples was determined using Hg intrusion porosimetry. The pore size distribution profile of both samples is shown in Figure S2 of the supplementary material. Both samples are essentially macroporous, the contribution of mesoporosity to the porous structure being very small. The macropore size distribution profile of both solids was bimodal, with maxima at 45.2 μm (most frequent pore diameter) and 32.9 μm for sample CF, whilst sample FF exhibited maxima at 17.2 μm and 11.3 μm (most frequent pore diameter). It is likely that the existence of inter particle spacing was the responsible for the large macropores obtained, especially in sample CF.

3.1.5. Microstructure.

SEM and TEM micrographs of the samples are displayed in Figures 4 and 5. The SEM images of sample CF, taken with a magnification of 15,000 \times and 30,000 \times , are depicted in Figures 4a and c. It showed the presence of aggregates with different shapes and sizes, consisting of a mixture of layered particle aggregates and particles with a rod-like morphology. The image also reveals the presence of inter particle cavities that are likely to be responsible for macroporosity. The enhanced resolution of TEM microscopy confirmed the heterogeneity of this solid, made of large particle aggregates and rod-like particles, as can be seen in the micrographs, shown in Figures 4b and d.

FIGURE 4

SEM and TEM images of sample FF are depicted in Figure 5a and c and 5b and d, respectively. The micrographs showed the presence of particle aggregates of different sizes, which led to the formation of a porous structure. The SEM micrograph also revealed the presence of inter particle cavities smaller than those of sample CF, which is in

agreement with the smaller macropore diameters (measured by Hg porosimetry) obtained for this sample.

FIGURE 5

TEM images allowed us to gain an in-depth knowledge of the microstructure of the materials. Thus, slit-shaped pores were identified in both dusts (Figure 4 b and 5 d), which is in accordance with the formation of the type H3 hysteresis loop. EDX analysis was used to determine the chemical composition of the rod-like particles, which confirmed the presence of iron, oxygen and calcium as the major constituent elements, the values in weight being 47%, 23% and 11%, respectively. This suggested that the rod-like particles are hematite aggregates.

3.1.6. *Thermal Analysis*

TGA and DTG curves of samples CF and FF are shown in Figure 6. The curves showed that the mass loss is a stepwise process. Both samples underwent mass loss, the percentage being 2.1% for sample CF and 2.5% for FF, corresponding to the DTG peak at 100°C, due to the loss of adsorbed moisture. A slight endothermic effect from 220 to 380°C (mass loss < 1.5%) can be due to the removal of water present in the structure of hydrated carbonates (Frost et al, 1999) and its partial loss in silicates (Boudonnet, 1994; Hornain et al., 1995). A third mass loss with DTG peak at 430°C, which corresponded to mass losses of 1% for sample CF and 2.4% for FF, can be attributed to dehydration of different hydroxides, mainly those of iron and magnesium (Setién et al., 2009). The large endothermic reaction with DTG peak at 770°C is due to dehydroxylation of Ca(OH)₂ to lime, and dehydration of the silicates present in the samples; the mass losses corresponding to this step are 4.6% for sample CF and 7.5% for sample FF. Finally, the

endothermic decomposition of carbonates with CO₂ evolution takes place, as well as the total dehydration of silicates; the mass losses linked to this step are 3.1% for sample CF and 4.7% for sample FF. It is worth noting that the thermal behavior of both samples was quite similar, being slightly higher the mass loss corresponding to the dust fines.

FIGURE 6

3.2. Environmental behavior

3.2.1. Leaching of the main compounds present in CF and FF samples

As it was previously commented, the generation of primary dust and sludge amounts to 0.6 kg/t sinter on average (World Steel Association, 2010). In this sense, sample CF is almost completely reused, whereas sample FF is stored outdoors for longer periods of time. It is worthy to note that these sinter dusts are composed of alkali metals, alkaline earth metals, metals, but most importantly, heavy metals. Therefore, these by-products can cause an environmental impact, since their contact with rainfall can produce the leaching of these metals. For this reason, it is essential to study their environmental behavior in order to evaluate their potential riskiness.

Figure S3 and S4 of the supplementary material shows the concentration of the different elements leached in the simulated rainfall at 3 different L/S ratios (1.25, 2.5 and 10) for four different periods of time: 1 week, 1 month, 3 months and 6 months in the sample FF and CF, respectively. Based on these data, the specific leaching rates of the different elements found in samples CF and FF were determined (Figure 7).

FIGURE 7

These results, expressed as μg dissolved per g of dust and time unit (μg dissolved/ $(\text{g}_{\text{dust}} \cdot \text{d})$), proved to be independent of the employed L/S ratio (between 1.25 and 10) and the selected leaching time (from 1 week to 6 months) for both the coarse and the fine fraction, as can be found in the Supplementary Material (Figures S5 and S6). On viewing these data, it should be noted that alkali metals (K), alkaline earth metals (Ca, Mg) and sulphur (S) were leached more easily in comparison to heavy metals (Fe, Mn and Cu) and metals (Al). Thus, Ca was the element that was leached to a greatest extent in both FF and CF samples, the leaching rates being $0.75 \pm 0.01 \mu\text{g}/(\text{g}_{\text{FF}} \cdot \text{d})$ and $0.48 \pm 0.01 \mu\text{g}/(\text{g}_{\text{CF}} \cdot \text{d})$, respectively. Regarding the heavy metals, Fe was the one that showed the highest rate, achieving a value of $(1.8 \pm 0.1) \times 10^{-3} \mu\text{g}/(\text{g}_{\text{FF}} \cdot \text{d})$ and $(1.13 \pm 0.04) \times 10^{-3} \mu\text{g}/(\text{g}_{\text{CF}} \cdot \text{d})$ for samples FF and CF, respectively. In the case of Mn, the leaching rate achieved was: $(4.99 \pm 0.09) \times 10^{-4} \mu\text{g}/(\text{g}_{\text{FF}} \cdot \text{d})$ for sample FF and $(3.7 \pm 0.4) \times 10^{-4} \mu\text{g}/(\text{g}_{\text{CF}} \cdot \text{d})$ for sample CF. Considering Cu, it was only found in sample FF and showed the lowest rate: $(1.20 \pm 0.1) \times 10^{-4} \mu\text{g}/(\text{g}_{\text{FF}} \cdot \text{d})$. Regarding metals, the leaching rate of Al was within the range of Cu and Mn leaching rates, the value being $(2.41 \pm 0.07) \times 10^{-4} \mu\text{g}/(\text{g}_{\text{FF}} \cdot \text{d})$ for sample FF and $(1.95 \pm 0.09) \times 10^{-4} \mu\text{g}/(\text{g}_{\text{CF}} \cdot \text{d})$ for sample CF. It should be noted that the leaching rates obtained were low in all cases, in particular for metals and heavy metals, thus, showing the minimum environmental impact of the leaching of the components of sinter dusts. For a better understanding of their potential riskiness, the volume of water that can be polluted by 1 ton of sinter dust due to the leaching of the heavy metals (Cu and Mn) and metals (Al) in a year was calculated (see Table S1 of the supplementary material). For determining this volume, the most restrictive toxicity values of different aquatic organisms, i.e. the lowest values of LC_{50} reported, and the specific leaching rates of Cu, Mn and Al in both fine and coarse fractions were used (eq. 1):

$$V = 365 \cdot 10^3 \cdot \frac{SLR}{LC_{50}} \quad (1)$$

Where, V is the volume in m³, SLR is the specific leaching rate in µg_{element}/(g_{dust}·d) of Cu, Mn or Al, and LC₅₀ is the concentration of Cu, Mn or Al that causes the death of 50% of the aquatic organisms in µg/L.

The toxicity values (LC₅₀) for the aquatic organisms (*Daphnia magna*, rainbow trout and coho salmon) varied from 4.8 to 33 µg/L; 1000 to 2200 µg/L and 500 to 2194 µg/L, for Cu, Mn and Al, respectively (Akira et al., 2015; EPA, 2007; Reimer, 1999; Gundersen et al., 1994; Buhl and Hamilton, 1991). In the worst case-scenario, the one corresponding to the lowest LC₅₀ value, the volume of water polluted by 1 ton of the fine fraction over 1 year was approximately 9.1 m³ for Cu and 0.2 m³ for Mn and Al (Table S1), whereas the values linked to the coarse fraction were lower (~0.1 m³ for both Mn and Al). Therefore, in this case, the riskiness associated with the leaching of sinter dust can be categorized as low. Nevertheless, the leaching behavior can also be affected by the surrounding environment. Thus, acidic or slightly acidic environments can increase the leachability of sinter dust constituents.

As can be seen from Figure 7, the particle size affected significantly the specific leaching rate of the elements, especially for Ca, K, S and Fe. Thus, the fine fraction exhibited higher rates than the coarse one (sample CF) due to its higher surface to volume ratio. For instance, the rate for K in sample CF was 0.13 ± 0.01 µg/(g_{dust}·d), this value being around 3.8 times higher in sample FF.

The only element with similar leaching rates for both fractions was Mg. This can be explained considering that the amount of Mg in sample CF is around 3 times higher than

in sample FF, which compensates for the lower surface to volume ratio of the former (see section related to chemical composition).

It should be also noted that Br was identified only in sample FF, and its leaching behavior differed from the rest of the elements, since it did not follow a linear trend with time. Thus, fast leaching was observed for the first days and then the values reaches a plateau. The amount of Br leached per gram of sample FF was successfully fitted ($R^2 = 0.99$) to the following equation (eq. 2):

$$\mu g_{dissolved} / g_{FF} = \frac{A \cdot t}{B + t} \quad (2)$$

Where: “A” is the maximum amount of Br leached per gram of FF, “B” is the time required to achieve half of the A value and “t” is time in days.

It was found that the amount leached per gram of FF was independent of the L/S ratio (Figure S7 of the supplementary material). Based on the fitting parameters obtained, 1.7 μg of Br were leached by each gram of fine dust at maximum, and around 55 days are required to dissolve half of this amount.

Conclusions

Sinter dusts (coarse and fine fractions) are highly heterogeneous and crystalline materials made up of hematite ($24.20 \pm 0.03\%$ for CF and $34.9 \pm 0.1\%$ for FF), sepiolite ($26.85 \pm 0.05\%$ for CF and $18.0 \pm 0.2\%$ for FF) and calcite ($17.9 \pm 0.1\%$ for CF and $10.48 \pm 0.02\%$ for FF). In the fine fraction, portlandite was also identified as a major phase ($10.37 \pm 0.03\%$).

Regarding textural properties, both dust fractions are basically macroporous materials, with specific surface area values of $21.6 \text{ m}^2/\text{g}$ for the coarse fraction and $33.7 \text{ m}^2/\text{g}$ for

dust fines. Their microstructures revealed the presence of particle aggregates of different sizes and inter particle cavities. Besides, rod-like particles, which can be attributed to hematite aggregates, were also distinguished in the coarse fraction.

The environmental behavior associated with dust particles accumulated in disposal areas under different simulated rainfall scenarios showed that the amount of element dissolved per g of dust and time unit ($\mu\text{g dissolved}/(\text{g}_{\text{dust}} \cdot \text{d})$), was the same regardless of the employed L/S ratio (between 1.25 and 10) and the selected leaching time (from 1 week to 6 months). Calcium, which can be regarded as non-toxic, was the element which exhibited the greatest leaching rates in both fine and coarse fractions. On the other hand, Fe showed the highest rate among the studied heavy metals also in both fractions this fact being less of a concern due to its inherent low toxicity compared to the other heavy metals (Al, Cu and Mn) present in sinter dusts. According to these results, the leaching of sinter dusts constituents caused a minimum environmental impact reverting in no further actions prior to its disposal.

Acknowledgements

This work was financed by Instituto de Desarrollo Económico del Principado de Asturias (IDEPA) and ArcelorMittal through the proof of concept SP-PA-15-RIS3-1. The technical assistance of the Scientific-Technical Services of the University of Oviedo is gratefully acknowledged.

References

Akira, O., Masumi, Y. and Norihisa, T., 2015. Acute toxicity of 50 metals to *Daphnia magna*. J. Appl. Toxicol. 35, 824-830.

Barret, E.P., Joyner, L.G., Halenda, P.P., 1951. The determination of pore volume and area distributions in porous substances. I. Computations from nitrogen isotherms. *J. Am. Chem. Soc.* 73, 3155–3158.

Bohidar, S.K., Naik, K.S., Sen, P.K., 2015. Role of electrostatic precipitator in industry. *Int. J. Adv. Res. Sci. Eng.* 4, 53-58.

Boudonnet, J.Y., 1994. Les laitiers d'aciérie LD: la caractérisation "chimie": une étape indispensable. *Panorama des connaissances. Lait. sidérurgiques* 76, 27–46.

Buhl, K.J., Hamilton, S.J., 1991. Relative sensitivity of early life stages of Arctic grayling, coho salmon, and rainbow trout to nine inorganics. *Ecotoxic. Environ. Safe.* 22, 184-197.

Brunauer, S., Deming, L.S., Deming, W.S., Teller, E., 1940. On a theory of the Van der Waals adsorption of gases. *J. Am. Chem. Soc.* 62, 1723–1732.

Chang, F., Wu, S., Zhang, F., Lu, H., Du, K., 2015. Characterization of Sintering Dust, Blast Furnace Dust and Carbon Steel Electric Arc Furnace Dust, in: *Characterization of Minerals, Metals, and Materials 2015*, John Wiley & Sons, Inc. 83-90.

Chukanov, N.V., Chervonnyi, A.D., 2016. *Infrared Spectroscopy of Minerals and Related Compounds*, first ed. Springer Mineralogy series. Springer International Publishing. Switzerland.

Dheilly, R.M., Tudo, J., Sebaïbi, Y. and Quéneudec, M., 2002. Influence of storage conditions on the carbonation of powdered Ca(OH)₂. *Constr. Build. Mater.* 16, 155-161.

Frost, H., Düren, T., Snurr, R.Q., 2006. Effects of surface area, free volume, and heat of adsorption on hydrogen uptake in metal–organic frameworks. *J. Phys. Chem. B.* 110, 9565-9570.

Frost, R.L., Horváth, E., Makó, E., Kristof, J., 2004. Modification of low and high-defect kaolinite surfaces: implications for kaolinite mineral processing. *J. Colloid Interface Sci.* 270, 337–346.

Frost, R.L., Kloprogge, J., Rusell, S.C., Szetu, J.L., 1999. Dehydroxylation and structure of alumina gels prepared from trisecbutoxyaluminium. *Thermochim. Acta* 329, 47–56.

Frost, R.L., Kristof, J., Paroz, N., Kloprogge, J.T., 1998. Role of water in the intercalation of kaolinite with hydrazine. *J. Colloid Interface Sci.* 208, 216–225.

Gridasov, V.P., Logachev, G.N., Pishnograev, S.N., Pavlov, A.V., Gostenin, V.A., Chevychelov, A.V., 2016. Behavior of Alkalis in Blast Furnaces. *Metallurgist* 59, 761-765.

Gundersen, D.T., Bustaman, S., Seim, W.K., Curtis, L.R., 1994. pH, hardness, and humic acid influence aluminum toxicity to rainbow trout (*Oncorhynchus mykiss*) in weakly alkaline waters. *Can. J. Fish. Aquat. Sci.* 51, 1345-1355.

Hornain, H., Rafai, N., Thuret, B., 1995. Contribution à la détermination de la chaux libre dans les laitiers LD: problèmes rencontrés, principales conditions. *Lait. Sidérurgiques* 78, 30–40.

Institute for Prospective Technological Studies Sustainable Production and Consumption Unit European IPPC Bureau, 2012. BREF Iron and Steel <http://eippcb.jrc.ec.europa.eu/reference/i&s.html> (accessed 13 March 2018).

Isik, M. and Gasanly, N.M., 2018. Trap characterization by photo-transferred thermoluminescence in MgO nanoparticles. *Physica B*. 537, 301-305.

Jovanovski, G., Makreski, P., Kaitner, B. and Boevd, B., 2009. Silicate Minerals from Macedonia. Complementary Use of Vibrational Spectroscopy and X-ray Powder Diffraction for Identification and Detection Purposes. *Croat. Chem. Acta*. 82, 363-386.

Katsnelson, B.A., Minigaliyeva, I.A., Panov, V.G., Privalova, L.I., Varaksin, A.N., Gurvich, V.B., Sutunkova, M.P., Shur, V.Y., Shishkina, E.V., Valamina, I.E., Makeyev, O.H., 2015. Some patterns of metallic nanoparticles' combined subchronic toxicity as exemplified by a combination of nickel and manganese oxide nanoparticles. *Food Chem. Toxicol.* 86, 351-364.

Krewski, D., Yokel, R.A., Nieboer, E., Borchelt, D., Cohen, J., Harry, J., Kacew, S., Lindsay, J., Mahfouz, A.M, Rondeau, V., 2017. Human health risk assessment for aluminium, aluminium oxide, and aluminium hydroxide. *J. Toxicol. Environ. Health B Crit. Rev.* 10, 1-269.

Lanzerstorfer, C., Steiner, D., 2016. Characterization of sintering dust collected in the various fields of the electrostatic precipitator. *Environ. Technol.* 37(12), 1559-1567.

Liang, X., Chi, J., Yang, Z., 2018. The influence of the functional group on activated carbon for acetone adsorption property by molecular simulation study. *Micropor. Mesopor. Mat.* 262, 77-88.

Ljung, K.S., Kippler, M.J., Goessler, W., Grandér, G.M., Nermell, B.M., Vahter, M.E., 2009. Maternal and early life exposure to manganese in rural Bangladesh. *Environ. Sci. Technol.* 43, 2595-2601.

López-Arce, P., Gómez-Villalba, L.S., Martínez-Ramírez, S., Álvarez de Buergo, M. Fort, R., 2011. Influence of relative humidity on the carbonation of calcium hydroxide nanoparticles and the formation of calcium carbonate polymorphs. *Powder Technol.* 205, 263-269.

Makreski, P., Jovanovski, G. and Kaitner, B., 2009. Minerals from Macedonia. XXIV. Spectra-structure characterization of tectosilicates. *J. Mol. Struct.* 924-926, 413-419.

Marks, B., Peters, A., McGough, D., 2017. Aquatic environmental risk assessment of manganese processing industries. *Neurotoxicology* 58, 187-193.

Mayo, D.W., Foil, A.M., Hannah, R.W 2004. *Course Notes on the Interpretation of Infrared and Raman Spectra*, Wiley-Interscience: New York, 316-318.

McKeown, D., E. Post, J. and S. Etz, E., 2002. Vibrational analysis of palygorskite and sepiolite. *Clay. Clay. Miner.* 50, 667-680.

Namduri, H., Nasrazadani, S., 2008. Quantative analysis of iron oxides using Fourier transform infrared spectrophotometry. *Corros. Sci.* 50, 2493–2497.

Navarro, C., Díaz, M., Villa-García, M.A., 2010. Physico-chemical characterization of steel slag. Study of its behavior under simulated environmental conditions. *Environ. Sci. Technol.* 44(14), 5383-5388.

Pelino, M., Karamanov, A., Pisciella, P., Crisucci, S., Zonetti, D., 2002. Vitrification of electric arc furnace dusts. *Waste Manag.* 22 (8), 945-949.

Peng, C., Guo, Z., Zhang, F., 2008. Discovery of potassium chloride in the sintering dust by chemical and physical characterization. *ISIJ International* 48(10), 1398-1403.

Peng, C., Guo, Z., Zhang, F., 2011. Existing state of potassium chloride in agglomerated sintering dust and its water leaching kinetics. *Trans. Nonferrous Met. Soc. China* 21(8), 1847-1854.

Queralt, I., Juliá, R., Plana, F., Bischoff, J. L., 1997. Anhydrous Ca-bearing magnesium carbonate from playa lake sediments, Salines Lake, Spain. *Am. Mineral.* 82, 812–819.

Rabah, M.A., 1999. Cost effectiveness of abatement options for emissions control in Egyptian iron foundries. *Waste Manag.* 19(4) 283-292.

Reimer, P.S., 1999. Environmental effects of manganese and proposed freshwater guidelines to protect aquatic life in British Columbia. MSc Thesis. Vancouver, University of British Columbia.

Remus, R., Aguado-Monsonet, M.A., Roudier, S., Delgado-Sancho, L., 2013. Best available techniques (BAT) reference document for iron and steel production. Industrial Emission Directive 2012/74/EU. Integrated Pollution Prevention and Control (IPPC). European Commission, Joint Research Centre, Institute for prospective technological studies, EU Publications, Luxemburg.

Reyes, V., Elholm, P., 2011. 4 generation of Coromax pulse generators for ESPs. ICESP XII Conference Papers, International Society for Electrostatic Precipitation (ISESP), Nürnberg, Germany.

Ritter, H., Ramm, J.H., Brühwiler, D., 2010. Influence of the structural properties of mesoporous silica on the adsorption of guest molecules. *Materials*. 3, 4500-4509.

Salama, W., El Aref, M. and Gaupp, R., 2015. Spectroscopic characterization of iron ores formed in different geological environments using FTIR, XPS, Mössbauer spectroscopy and thermoanalyses. *Spectrochim. Acta A*. 136, 1816-1826.

Saniger, J., 1995. Al-O infrared vibrational frequencies of γ -alumina. *Mater. Letter*. 22, 109-113.

Schroeder, P.A., 2002. Infrared spectroscopy in clay science: In CMS Workshop Lectures, Vol. 11, Teaching Clay Science, A. Rule and S. Guggenheim, eds., The Clay Mineral Society, Aurora, CO, 181-206.

Setién, J., Hernández, D., González, J.J., 2009. Characterization of ladle furnace basic slag for use as a construction material. *Constr. Build. Mater*. 2009, 23, 1788–1794.

Sinha, M., Ramna, R.V., Sinha, S., Bose, G., 2010. Characterisation of ESP dust sample from sinter plant. *ISIJ International* 50(11), 1719-1721.

Tang, H., Sun, W., Han, H., 2015. A novel method for comprehensive utilization of sintering dust. *Trans. Nonferrous Met. Soc. China* 25 (12), 4192-4200.

Taylor, J.C., 2001. Rietveld made easy: a practical guide to the understanding of the method and successful phase quantifications, Sietronics Pty Ltd: Canberra.

U.S. Environmental Protection Agency (EPA), 2007. Aquatic life ambient freshwater quality criteria – copper. Revision. EPA-822-R-07-001.

Van der Marel, H.W., Beutelspacher, H., 1976. Atlas of Infrared Spectroscopy of Clay Minerals and Their Admixtures, Elsevier: Amsterdam, 224-229.

Vehlow, J., 2015. Air pollution control systems in WtE units: An overview. Waste Manag. 37, 58-74.

World Steel Association, 2010. Steel industry by-products. Project group report 2007-2009. Brussels.

Xie, J., Bai, X., Lavoie, M., Lu, H., Fan, X., Pan, X., Fu, Z. and Qian, H., 2015. Analysis of the proteome of the marine diatom *Phaeodactylum tricornutum* exposed to aluminum providing insights into aluminum toxicity mechanisms. Environ. Sci. Technol. 49(18), 11182-11190.

Figure 1

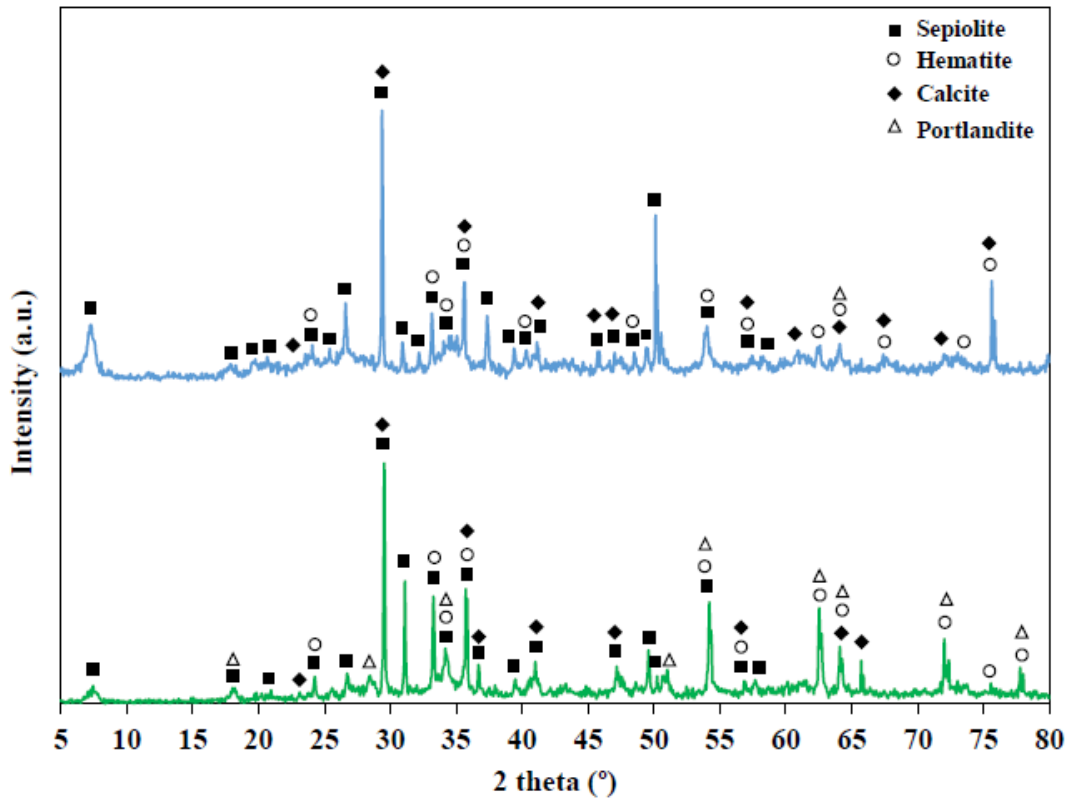


Figure 1. XRD patterns of sinter dust samples with the main phases (sepiolite, hematite, calcite and portlandite) identified: coarse fraction (CF) in blue dotted line and fine fraction (FF) in green solid line.

Figure 2

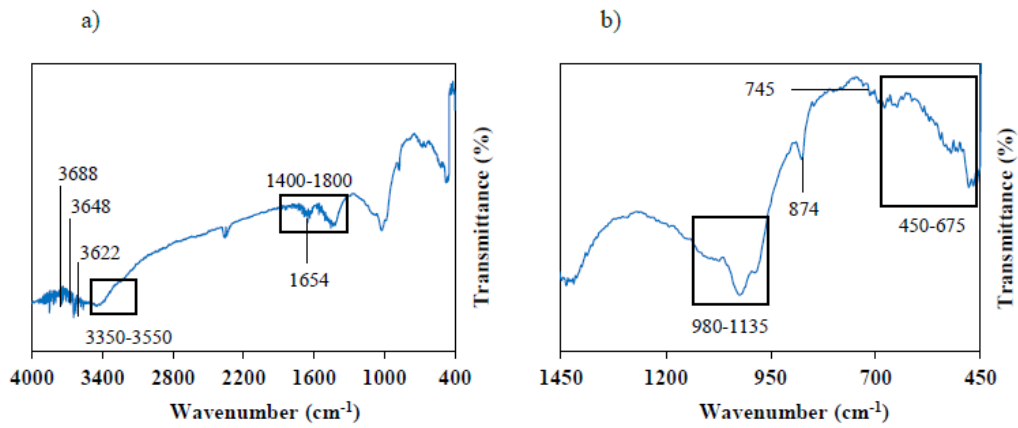


Figure 2. a) FTIR transmission spectrum of sinter dust coarse fraction (CF) from 400 to 4000 cm^{-1} . b) Zoom area of the FTIR spectrum from 450 to 1450 cm^{-1} .

Figure 3

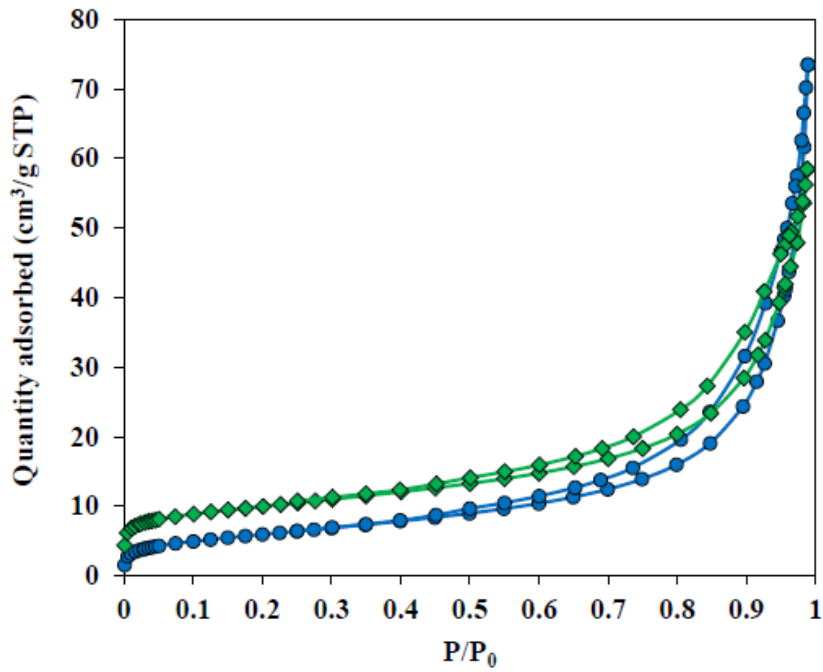


Figure 3. N₂ adsorption-desorption isotherms at 77 K of sinter dusts samples: (●) coarse fraction (CF) and (◆) fine fraction (FF).

Figure 4

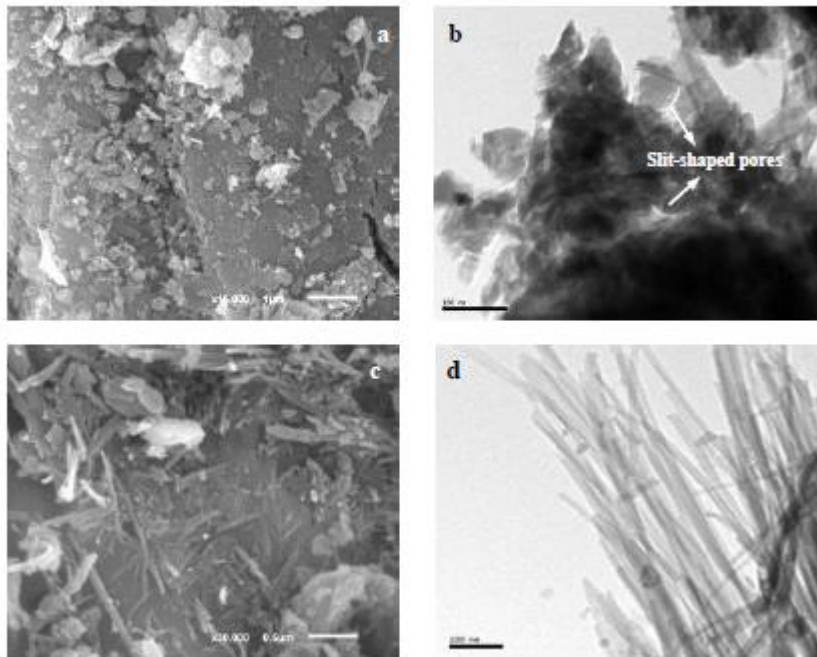


Figure 4. SEM micrographs of sinter dust coarse fraction (CF) taken by SEM at a magnification of 15,000× and 30,000× (a and c) and by TEM at a magnification of 150,000× and 100,000× (b and d).

Figure 5

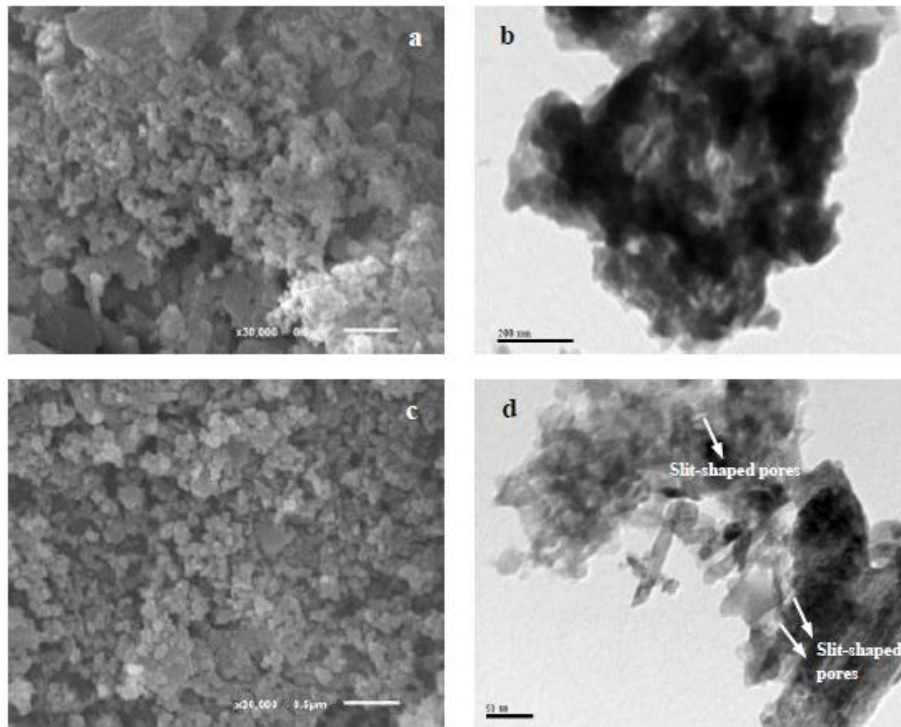


Figure 5. Micrographs of sinter dust fine fraction (FF) taken by SEM at a magnification of 30,000 \times (a and c) and by TEM at a magnification of 80,000 \times and 200,000 \times (b and d).

Figure 6

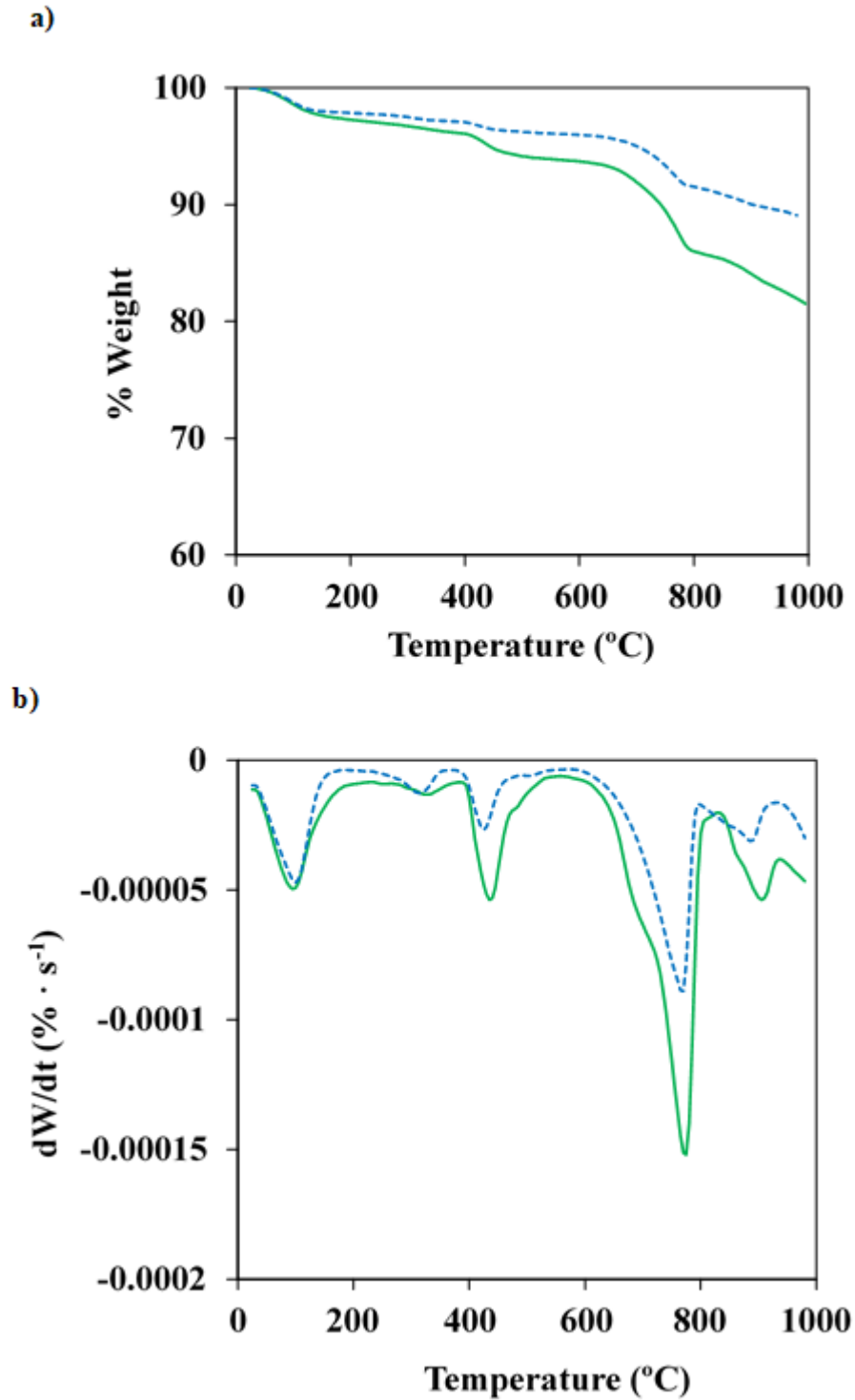


Figure 6. TG and DTA curves of sinter dust samples: coarse fraction (CF) in blue dotted line and fine fraction (FF) in green solid line.

Figure 7

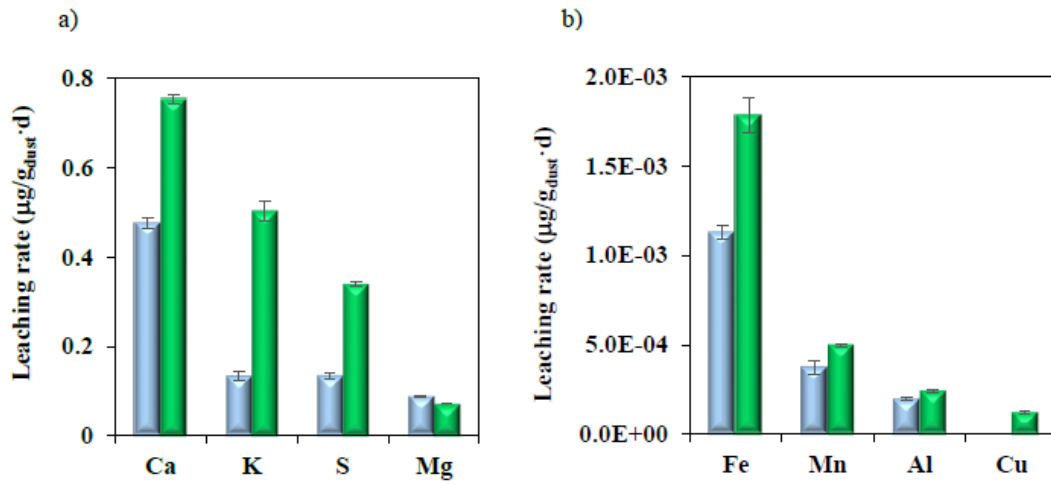


Figure 7. Specific leaching rates, $\mu\text{g}_{\text{element}}/(\text{g}_{\text{dust}}\cdot\text{d})$, of the elements found in sinter dust samples: (■) coarse fraction (CF) and (■) fine fraction (FF). a) Ca, K, S and Mg. b) Fe, Mn, Al and Cu (only present in sample FF).

Table 1. Elemental analysis of the sinter dusts samples: coarse fraction (CF) and fine fraction (FF)

	% N	% C	% S	% H
Sample CF	0.168 ± 0.004	3.67 ± 0.03	1.238 ± 0.005	0.213 ± 0.002
Sample FF	0.152 ± 0.006	11.74 ± 0.02	0.658 ± 0.003	0.243 ± 0.004

Table 2. Trace elements found in sinter dust samples measured by XRF: coarse fraction (CF) and fine fraction (FF)

Compound	Sample FF	Compound	Sample CF
MnO	0.323 % ± 0.006	K₂O	0.73 % ± 0.05
Sc₂O₃	0.191 % ± 0.006	MnO	0.343 % ± 0.004
Br	0.081 % ± 0.001	Tm₂O₃	0.179 % ± 0.002
ReO₂	0.074 % ± 0.003	SrO	0.031 % ± 0.002
Ac₂O₃	0.056 % ± 0.003		
CuO	0.044 % ± 0.004		
SrO	0.026 % ± 0.004		

Table 3. Major and minor phases of sinter dust samples determined by Rietveld method: coarse fraction (CF) and fine fraction (FF).

Sample FF		Sample CF	
Major phases	Percentage	Major phases	Percentage
Hematite (Fe ₂ O ₃)	34.9 ± 0.1%	Sepiolite (Mg ₈ Si ₁₂ (OH) ₂ ·12H ₂ O)	26.85 ± 0.05%
Sepiolite (Mg ₈ Si ₁₂ (OH) ₂ ·12H ₂ O)	18.0 ± 0.2%	Hematite (Fe ₂ O ₃)	24.20 ± 0.03 %
Calcite (CaCO ₃)	10.48 ± 0.02%	Calcite (CaCO ₃)	17.9 ± 0.1%
Portlandite Ca(OH) ₂	10.37 ± 0.03%	Minor phases	Percentage
Minor phases	Percentage	Dolomite CaMg(CO ₃) ₂	9.21 ± 0.06%
Quartz (SiO ₂)	6.33 ± 0.01%	Portlandite Ca(OH) ₂	7.52 ± 0.02%
Albite (NaAlSi ₃ O ₈)	5.75 ± 0.03%	Quartz (SiO ₂)	5.75 ± 0.01%
Dolomite CaMg(CO ₃) ₂	5.42 ± 0.04%	Albite (NaAlSi ₃ O ₈)	4.30 ± 0.04%
Sylvine (KCl)	3.0 ± 0.1%	Anhydrite (CaSO ₄)	1.44 ± 0.07%
Microcline (KAlSi ₃ O ₈)	2.24 ± 0.05%	Microcline (KAlSi ₃ O ₈)	1.20 ± 0.02%
Anhydrite (CaSO ₄)	2.25 ± 0.03%	Gibbsite Al(OH) ₃	1.11 ± 0.03%
Hedenbergite (CaFeSi ₂ O ₆)	1.26 ± 0.02%	Hedenbergite (CaFeSi ₂ O ₆)	0.52 ± 0.03%

Table 4. Textural parameters of the sinter dust samples obtained from the nitrogen adsorption–desorption isotherms at 77 K.

Sample	S_{BET} (m ² /g)	$D_{\text{p, max}}$ (nm)	V_{p} (cm ³ /g STP)
FF	33.7	13.1	0.088
CF	21.6	18.6	0.114

Supplementary Material to

**‘Characterization of sinter flue dust to enhance
alternative recycling and environmental impact at
disposal’**

*Victoria Masaguer^a, Paula Oulego^b, Sergio Collado^b, María A. Villa-García^c, and
Mario Díaz^{b,*}*

^aGlobal R&D Asturias Centre “GRID”, Apartado 90, 33400 Aviles, Spain

^bDepartment of Chemical and Environmental Engineering, University of Oviedo,

c/Julián Clavería s/n, E-33071, Oviedo, Spain

^cDepartment of Organic and Inorganic Chemistry, University of Oviedo

c/Julián Clavería s/n, E-33071, Oviedo, Spain

(9 Pages, 7 Figures, 1 Table)

Table of contents

- 1. FTIR spectrum of sample FF (Figure S1).**
- 2. Hg intrusion porosimetry of samples FF and CF (Figure S2).**
- 3. Concentration of leached elements from sample FF (Figure S3).**
- 4. Concentration of leached elements from sample CF (Figure S4).**
- 5. Results related to the specific leaching rates for sample FF (Figure S5).**
- 6. Results related to the specific leaching rates for sample CF (Figure S6).**
- 7. Volume of water that can be polluted by 1 ton of sinter dust in a year (Table S1).**
- 8. Results related to the leaching of Br for sample FF (Figure S7).**

Corresponding author’s e-mail: mariodiaz@uniovi.es

Phone: +34 985 10 34 39; Fax: +34 985 10 34 34

1. FTIR spectrum of sample FF (Figure S1).

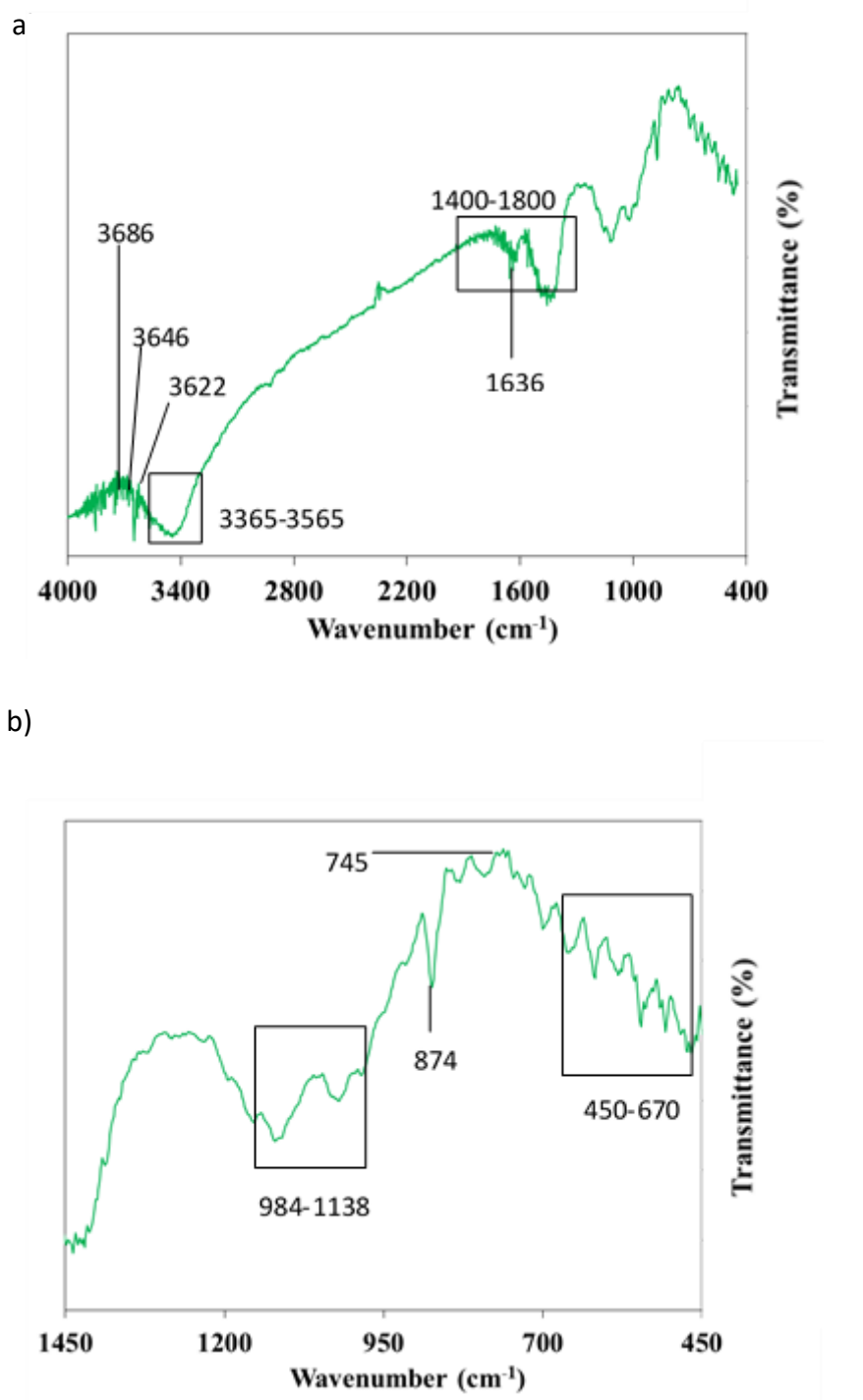
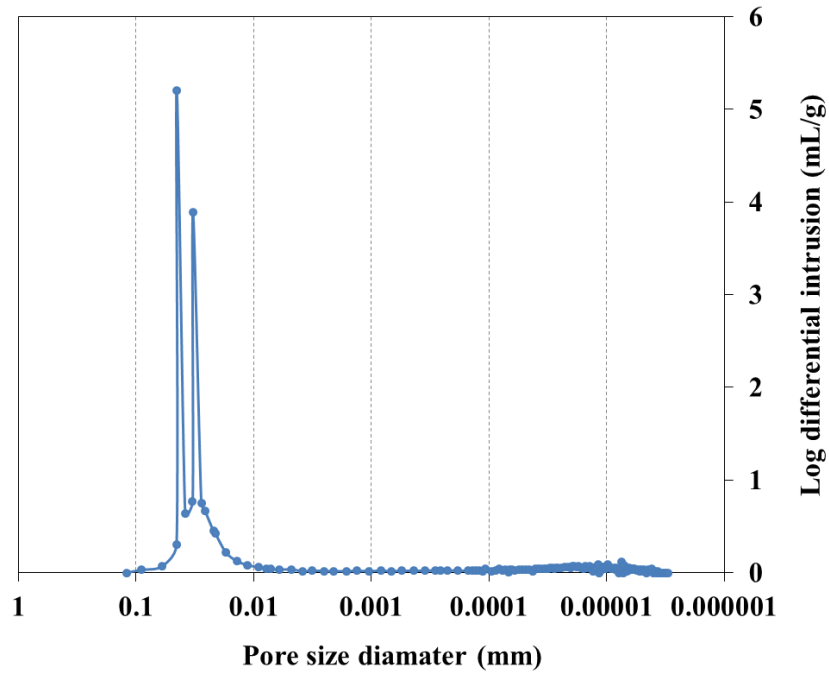


Figure S1. a) Full FTIR spectrum of sample FF. b) Zoom area of FTIR spectrum from 450 to 1450 cm⁻¹.

2. Hg intrusion porosimetry of samples FF and CF (Figure S2).

a)



b)

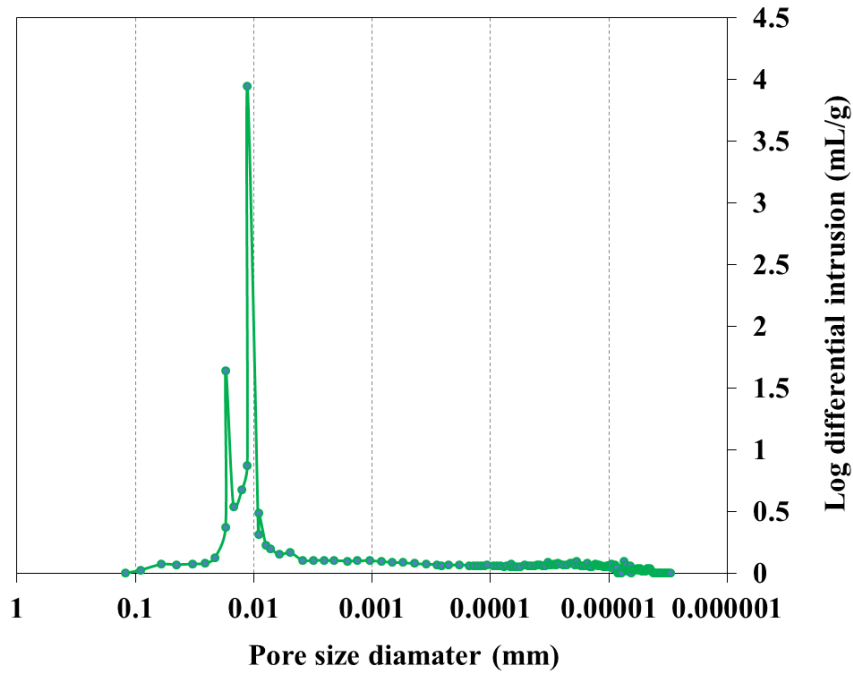


Figure S2. Pore size distribution profiles of sinter dusts measured by mercury intrusion porosimetry: a) sample CF and b) sample FF.

3. Concentration of leached elements from sample FF (Figure S3).

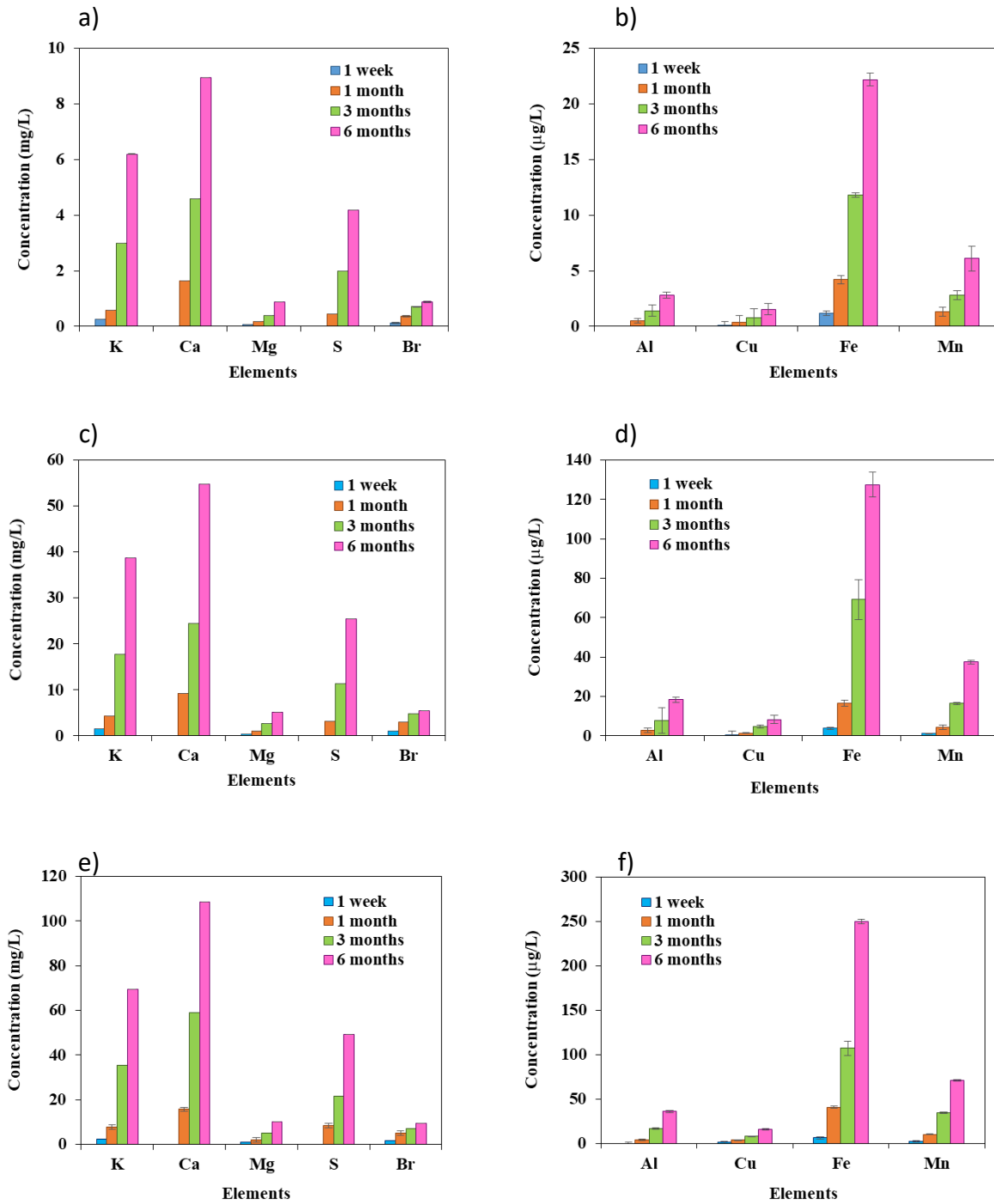


Figure S3. Concentration of the different elements leached from the sample FF in the simulated rainfall for four different periods of time: 1 week, 1 month, 3 months and 6 months at 3 different L/S ratios: a) and b) 10; c) and d) 2.5; and e) and f) 1.25. The concentration of Br has been multiplied by 10 to enhance the legibility of the figures.

4. Concentration of leached elements from sample CF (Figure S4).

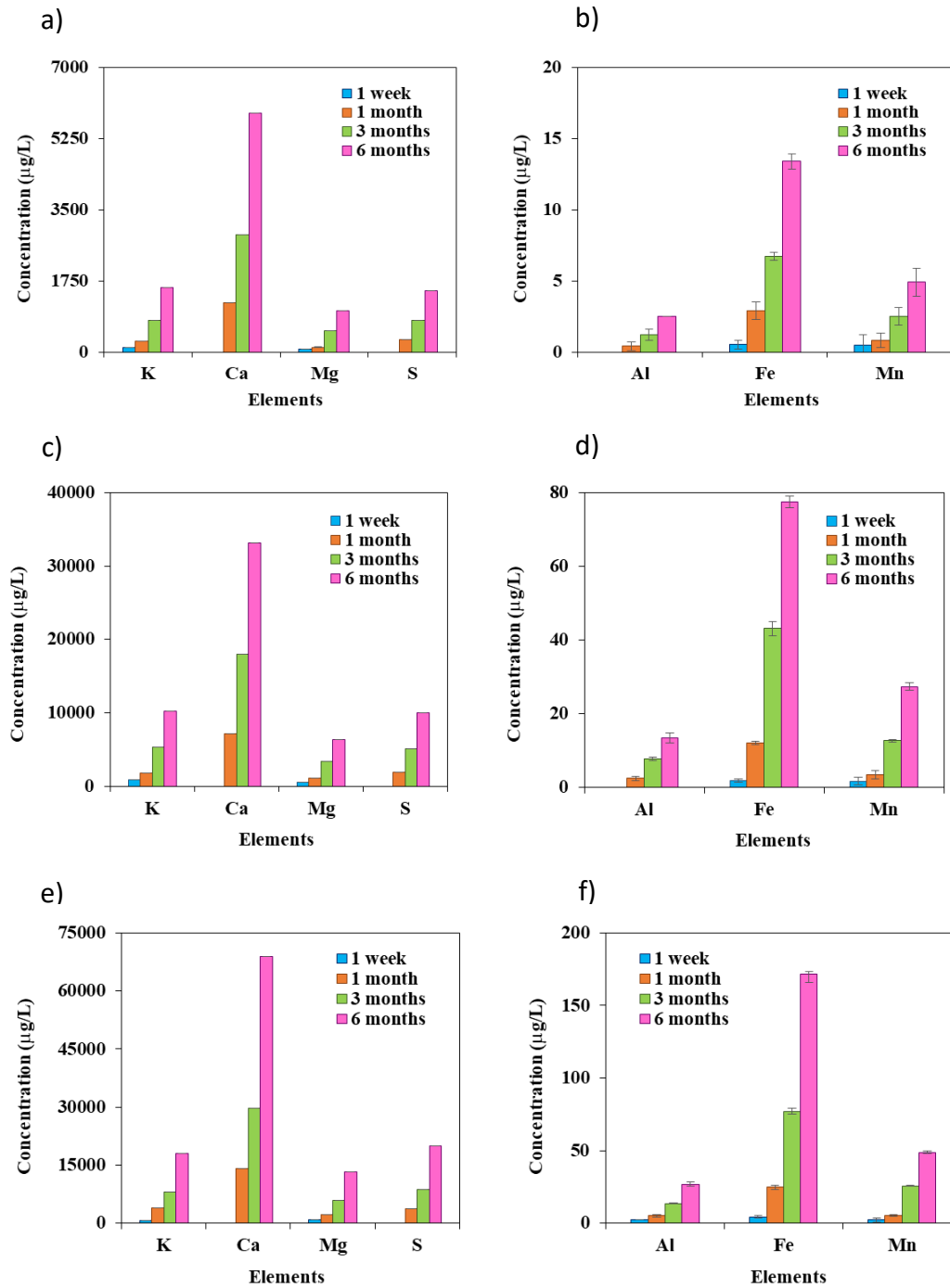


Figure S4. Concentration of the different elements leached from the sample CF in the simulated rainfall for four different periods of time: 1 week, 1 month, 3 months and 6 months at 3 different L/S ratios: a) and b) 10; c) and d) 2.5; and e) and f) 1.25.

5. Results related to the specific leaching rates for sample FF (Figure S5).

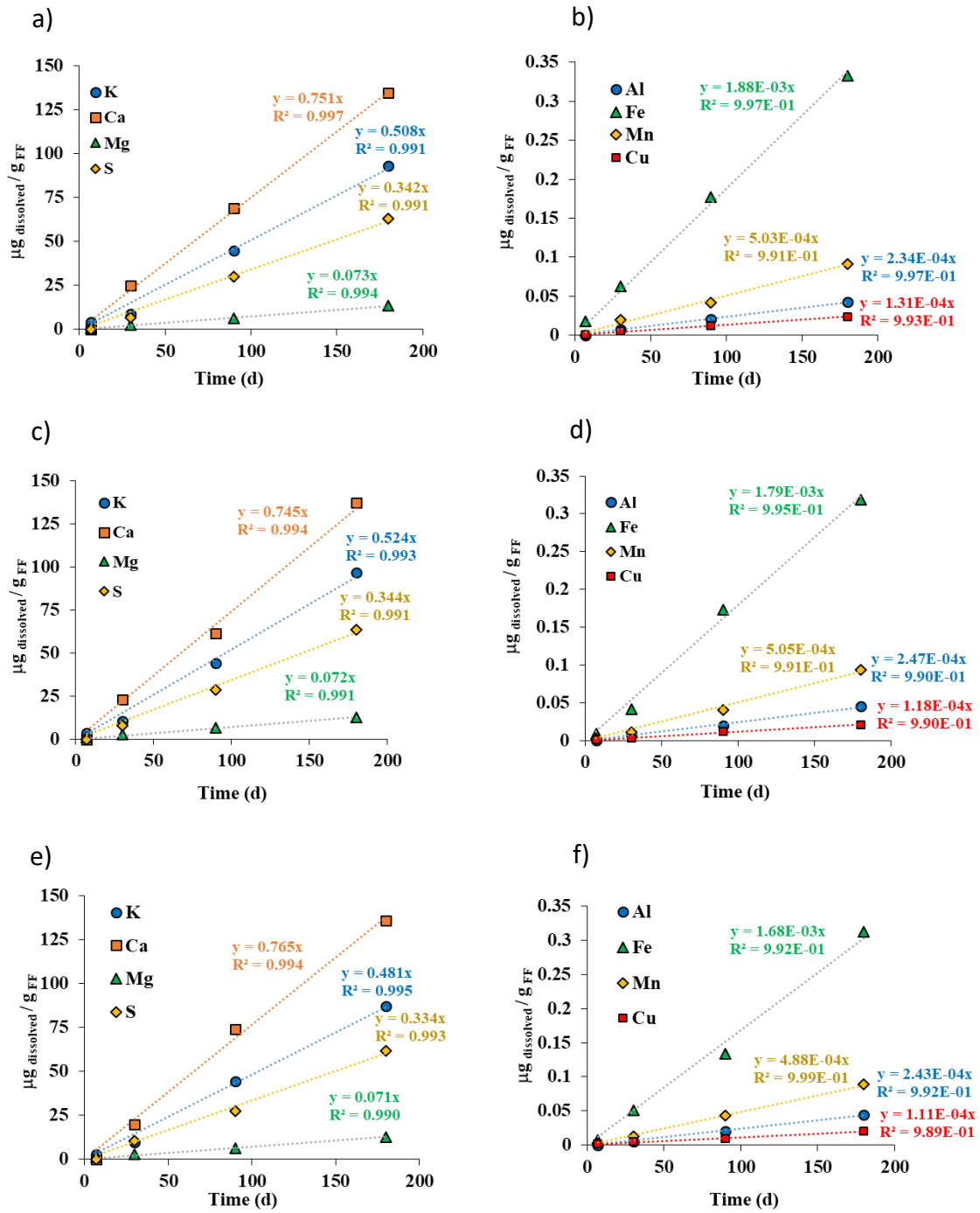


Figure S5. Evolution of the amount of $\mu\text{g}_{\text{dissolved}}/\text{g}_{\text{FF}}$ with time for the different elements leached from the sample FF at L/S ratios: a) and b) 10; c) and d) 2.5; and e) and f) 1.25. The value of the slope in each of the linear fittings is the specific leaching rate.

6. Results related to the specific leaching rates for sample CF (Figure S6).

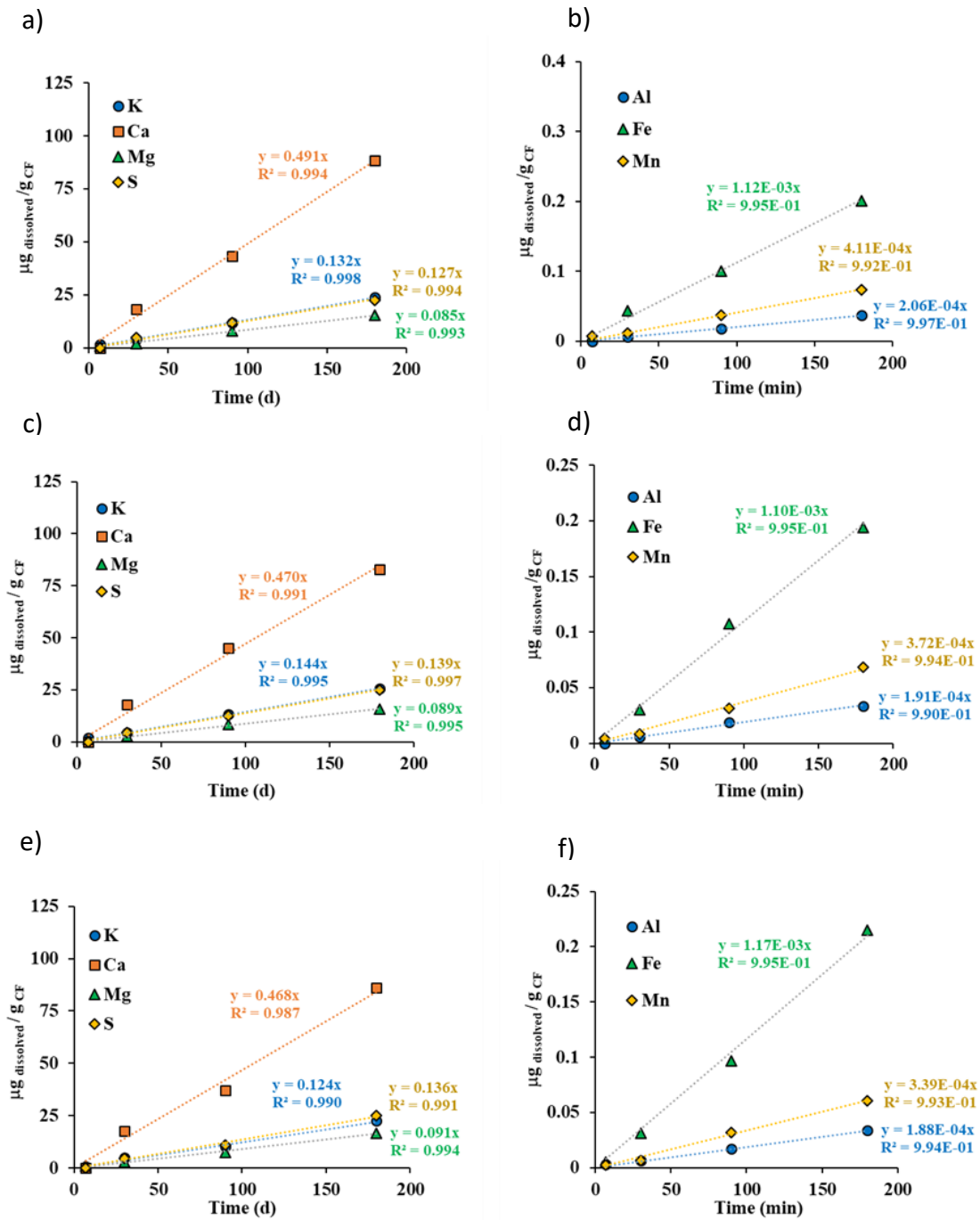


Figure S6. Evolution of the amount of $\mu\text{g dissolved/g CF}$ with time for the different elements leached from the sample CF at L/S ratios: a) and b) 10; c) and d) 2.5; and e) and f) 1.25. The value of the slope in each of the linear fittings is the specific leaching rate.

7. Volume of water that can be polluted by 1 ton of sinter dust in a year (Table S1).

Table S1. Volume of water that can be polluted by 1 ton of sinter (fine and coarse fractions) due to the leaching of Cu, Mn and Al over a year.

	Fine fraction (sample FF)					
	LC _{50, Cu} (µg/L)	V _{Cu} (m ³) ^a	LC _{50, Mn} (µg/L)	V _{Mn} (m ³) ^b	LC _{50, Al} (µg/L)	V _{Al} (m ³) ^c
<i>Daphnia magna</i>	4.8	9.1	1000	0.18	930	0.10
Rainbow trout	17.0	2.6	2000	0.09	2194	0.04
Coho salmon	33.0	1.3	2200	0.08	500	0.18

	Coarse fraction (sample CF)					
	LC _{50, Cu} (µg/L)	V _{Cu} (m ³) ^d	LC _{50, Mn} (µg/L)	V _{Mn} (m ³) ^e	LC _{50, Al} (µg/L)	V _{Al} (m ³) ^f
<i>Daphnia magna</i>	4.8	n.a.	1000	0.14	930	0.08
Rainbow trout	17.0	n.a.	2000	0.07	2194	0.03
Coho salmon	33.0	n.a.	2200	0.07	500	0.14

Specific leaching rates (SLR): a= $(1.20 \pm 0.1) \times 10^{-4} \mu\text{g}_{\text{Cu}}/(\text{g}_{\text{FF}} \cdot \text{d})$; b= $(4.99 \pm 0.09) \times 10^{-4} \mu\text{g}_{\text{Mn}}/(\text{g}_{\text{FF}} \cdot \text{d})$;

c= $(2.41 \pm 0.07) \times 10^{-4} \mu\text{g}_{\text{Al}}/(\text{g}_{\text{FF}} \cdot \text{d})$; d= element not identified;

e= $(3.7 \pm 0.4) \times 10^{-4} \mu\text{g}_{\text{Mn}}/(\text{g}_{\text{CF}} \cdot \text{d})$; f= $(1.95 \pm 0.09) \times 10^{-4} \mu\text{g}_{\text{Al}}/(\text{g}_{\text{CF}} \cdot \text{d})$

8. Results related to the leaching of Br for sample FF (Figure S7).

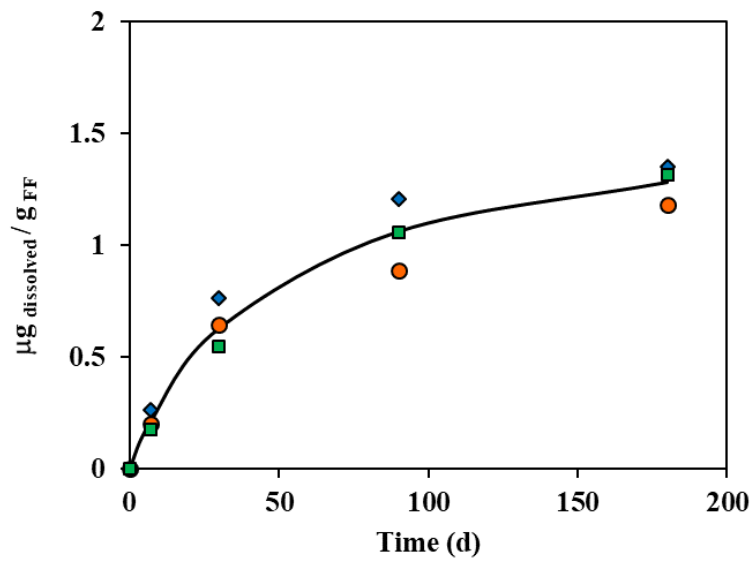


Figure S7. Evolution of the amount of $\mu\text{g}_{\text{dissolved}}/\text{g}_{\text{FF}}$ of Br with time at different L/S ratios:

10 (■), 2.5 (◆) and 1.25 (●).